Robust Subspace Identification of a Nonlinear Satellite Using Model Reduction

T. Dossogne, J.P. Noël, G. Kerschen

Space Structures and Systems Laboratory (S3L)
Aerospace and Mechanical Engineering Department
University of Liège, Liège, Belgium
tdossogne, jp.noel, g.kerschen@ulg.ac.be

ABSTRACT

The frequency-domain nonlinear subspace identification (FNSI) method has recently been successfully applied to large-scale nonlinear structures. One of the key features of FNSI is the nonlinear generalisation of the stabilisation diagram. However, as in linear system identification, the selection of the model order in the diagram is complicated by the presence of spurious poles, resulting from noise and modelling errors. Spurious poles have been shown to strongly perturb the estimation of the nonlinear coefficients.

The present paper establishes a constructive procedure to discriminate between spurious and genuine poles. This procedure is derived in modal space and is based on a dominancy index and on model reduction techniques. It is demonstrated on a complete satellite structure possessing nonsmooth nonlinearities and high modal density. Spurious frequency variations in the nonlinear coefficients are proved to be effectively removed, significantly improving the quality of the overall identified model.

Keywords: subspace method, nonlinear system identification, satellite structure, modal dominancy index, spurious poles, nonsmooth nonlinearities.

1 INTRODUCTION

Satellite structures are most often made of different subsystems assembled through joints that can exhibit nonlinear behaviour. Indeed, those connections may be prone to softening, friction or gaps and hence strongly impact the overall satellite dynamics[1] [2] [3]. Moreover, due to their extreme operating conditions, such as launch or space environment constraints, satellites are submitted to high amplitude oscillations, which tends to increasingly trigger those nonlinear mechanisms. Such complex phenomena can even jeopardize the structural integrity of the satellite[4] [5].

Therefore, investigating the nonlinear dynamics of space structures has become of great interest[6]. In this context, the application of a frequency-domain subspace identification method, termed FNSI[7], has shown promising results to identify nonlinear space systems[8] [9].

However, as far as large-scale engineering structures are concerned, high modal density, complex dynamics and noise can complicate the identification process. More specifically, the model order selection and the nonlinear parameter estimation in presence of spurious poles remain challenging tasks.

The objective of this paper is thus to improve the FNSI method in order to accurately identify a satellite structure whose specific connections and mounting devices introduce strongly nonlinear behaviour in the dynamics. Improvements of the method are carried out by introducing techniques to cope with the described difficulties. On the one hand, a tool for a robust and straightforward selection of the model order is proposed and, on the other hand, an automatic procedure to identify and extract spurious poles is integrated to FNSI.

The paper is organized as follows. The frequency-domain subspace identification method is first introduced in Section 2. Then, an information criterion establishing the best accommodation between a weak model error and a low noise sensitivity is developed in Section 3. Next, Section 4 addresses the problem of spurious poles and, a strategy to automatically discard them by means of a modal dominancy index is proposed. In Section 5, the satellite structure is first described before addressing its numerical modelling and finally the robust subspace identification of the complete satellite is performed.

2 FREQUENCY-DOMAIN NONLINEAR SUBSPACE IDENTIFICATION

In the present section, the frequency-domain subspace identification technique is presented. It is applicable to multi-input, multi-output structures with high damping and high modal density, and makes no assumption as to the importance of nonlinearity in the measured dynamics. The main steps of the method are presented hereafter.

2.1 NONLINEAR MODEL EQUATIONS IN THE PHYSICAL SPACE

The vibrations of nonlinear systems obey Newton's second law of dynamics

$$\mathbf{M}\,\ddot{\mathbf{q}}(t) + \mathbf{C}_v\,\dot{\mathbf{q}}(t) + \mathbf{K}\,\mathbf{q}(t) + \mathbf{f}(\mathbf{q}(t),\dot{\mathbf{q}}(t)) = \mathbf{p}(t) \tag{1}$$

where $\mathbf{C}_v \in \mathbb{R}^{\,n_p\times n_p}$ is the linear viscous damping matrix; $\mathbf{p}(t) \in \mathbb{R}^{\,n_p}$ is the generalized external force vector; $\mathbf{f}(\mathbf{q}(t),\dot{\mathbf{q}}(t)) \in \mathbb{R}^{\,n_p}$ is the nonlinear restoring force vector encompassing elastic and dissipative terms. The nonlinear restoring force term in Eq. (1) is expressed by means of a linear combination of known basis functions $\mathbf{h}_a(\mathbf{q}(t),\dot{\mathbf{q}}(t))$ as

$$\mathbf{f}(\mathbf{q}(t),\dot{\mathbf{q}}(t)) = \sum_{a=1}^{s} c_a\,\mathbf{h}_a(\mathbf{q}(t),\dot{\mathbf{q}}(t)). \tag{2}$$

In this sum, the coefficients c_a associated with the nonlinear basis functions $\mathbf{h}_a(\mathbf{q}(t),\dot{\mathbf{q}}(t))$ play a role similar to the linear stiffness and viscous damping coefficients contained in the matrices $\mathbf{K}$ and $\mathbf{C}_v$ in Eq. (1), respectively.

2.2 FEEDBACK INTERPRETATION AND STATE-SPACE MODEL EQUATIONS

The FNSI approach builds on a block-oriented interpretation of nonlinear structural dynamics, which sees nonlinearities as a feedback into the linear system in the forward loop [10], as illustrated in Fig. 1. This interpretation boils down to moving the nonlinear internal forces in Eq. (1) to the right-hand side, and viewing them as additional external forces applied to the underlying linear structure, that is,

$$\mathbf{M}\,\ddot{\mathbf{q}}(t) + \mathbf{C}_v\,\dot{\mathbf{q}}(t) + \mathbf{K}\,\mathbf{q}(t) = \mathbf{p}(t) - \sum_{a=1}^{s} c_a\,\mathbf{h}_a(\mathbf{q}(t),\dot{\mathbf{q}}(t)). \tag{3}$$

Without loss of generality, it is assumed in this section that the structural response is measured in terms of generalized displacements. Defining the state vector $\mathbf{x} = \left(\mathbf{q}^T \;\; \dot{\mathbf{q}}^T\right)^T \in \mathbb{R}^{\,n_s}$, where $n_s = 2\,n_p$ is the dimension of the state space and T the matrix transpose, Eq. (3) is recast into the set of first-order equations

$$\left\{ \begin{array}{lcl} \dot{\mathbf{x}}(t) & = & \mathbf{A}\,\mathbf{x}(t) + \mathbf{B}\,\mathbf{e}(t) \\ \mathbf{q}(t) & = & \mathbf{C}\,\mathbf{x}(t) + \mathbf{D}\,\mathbf{e}(t) \end{array} \right. \tag{4}$$

where the vector $\mathbf{e} \in \mathbb{R}^{\,(s+1)\,n_p}$, termed *extended input vector*, concatenates the external forces $\mathbf{p}(t)$ and the nonlinear basis functions $\mathbf{h}_a(t)$. The matrices $\mathbf{A} \in \mathbb{R}^{\,n_s\times n_s}$, $\mathbf{B} \in \mathbb{R}^{\,n_s\times(s+1)\,n_p}$, $\mathbf{C} \in \mathbb{R}^{\,n_p\times n_s}$ and $\mathbf{D} \in \mathbb{R}^{\,n_p\times(s+1)\,n_p}$ are the state, extended input, output and direct feedthrough matrices, respectively. State-space and physical-space matrices correspond through the relations

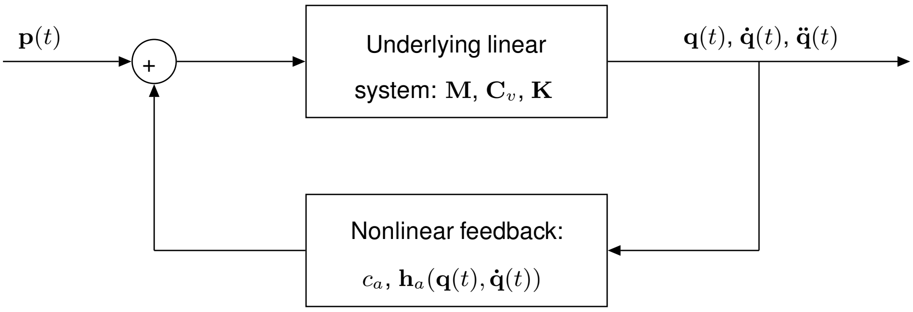

Figure 1: Feedback interpretation of nonlinear structural dynamics.

$$\mathbf{A} = \begin{pmatrix} \mathbf{0}^{\,n_p \times n_p} & \mathbf{I}^{\,n_p \times n_p} \\ -\mathbf{M}^{-1}\,\mathbf{K} & -\mathbf{M}^{-1}\,\mathbf{C}_v \end{pmatrix} \; ; \quad \mathbf{B} = \begin{pmatrix} \mathbf{0}^{\,n_p \times n_p} & \mathbf{0}^{\,n_p \times n_p} & \mathbf{0}^{\,n_p \times n_p} & \dots & \mathbf{0}^{\,n_p \times n_p} \\ \mathbf{M}^{-1} & -c_1\,\mathbf{M}^{-1} & -c_2\,\mathbf{M}^{-1} & \dots & -c_s\,\mathbf{M}^{-1} \end{pmatrix}$$
$$\mathbf{C} = \begin{pmatrix} \mathbf{I}^{\,n_p \times n_p} & \mathbf{0}^{\,n_p \times n_p} \end{pmatrix} \; ; \quad \mathbf{D} = \mathbf{0}^{\,n_p \times (s+1)\,n_p} \tag{5}$$

Given measurements of $\mathbf{p}(t)$ and $\mathbf{q}(t)$, and an appropriate selection of the model order n_s and the functionals $\mathbf{h}_a(t)$, the FNSI method delivers the four state space matrices $\mathbf{A}$, $\mathbf{B}$, $\mathbf{C}$ and $\mathbf{D}$ using a classical subspace resolution scheme in the frequency domain. The identified state-space model $(\mathbf{A}, \mathbf{B}, \mathbf{C}, \mathbf{D})$ can then be converted into physical and modal space to estimate both the nonlinear coefficients c_a and the underlying linear modal properties of the system. Detailed description of the subspace resolution scheme and the conversion from state space to physical space can be found in [7].

3 MODEL ORDER SELECTION

The selection of an appropriate model order is far form being trivial, especially when real data are concerned. Indeed, for low orders, as a few modes are identified, the error made by the model is big. However, for high model orders, the error decreases and tends to converge as the added poles are either corresponding to low-contribution modes, either spurious. Therefore, there exists an optimal order in comparison with which higher orders do not improve significantly the quality of the model. Moreover, despite their important computational cost, too high orders tend to make the model more sensitive to noise and are therefore to avoid.

Given an initial state and the four computed state space matrices for a specific order n_s, it is possible to simulate the response of the estimated system using Eq. (6). For this purpose, the state matrices $\mathbf{A}$ and $\mathbf{B}$ are first converted into their discrete-time form using $\mathbf{A}_d = \mathrm{expm}\,(\mathbf{A}/f_s)$ and $\mathbf{B}_d = \left(\mathrm{expm}\,(\mathbf{A}/f_s) - \mathbf{I}^{n_s \times n_s}\right)\mathbf{A}^{-1}\mathbf{B}$ where f_s is the sampling frequency.

$$\left\{ \begin{array}{rcl} \hat{\mathbf{x}}(t_k+1) & = & \mathbf{A}_d\,\hat{\mathbf{x}}(t_k) + \mathbf{B}_d\,\mathbf{e}(t_k) \\ \hat{\mathbf{y}}(t_k) & = & \mathbf{C}\,\hat{\mathbf{x}}(t_k) + \mathbf{D}\,\mathbf{e}(t_k) \end{array} \right. \tag{6}$$

The quality of the estimation for that specific model order can hence be assessed by comparing the simulated output $\hat{\mathbf{y}}$ with the real measured output. A model error is defined as

$$\mathbf{V}(n_s) = \|\hat{\mathbf{Y}}^{ss}(\omega) - \mathbf{Y}(\omega)\|_2 \tag{7}$$

where $\hat{\mathbf{Y}}^{ss}$ is the Fourier transform of the simulated output $\hat{\mathbf{y}}$ in steady-state. An information criterion is proposed in Eq. (8). It is based on the formulation of the *Akaike Information Criterion* in frequency-domain [11][12] where the cost function of the maximum likelihood estimation is here replaced by the model error $\mathbf{V}$, while the second factor introduces a penalty related to increasing the order.

$$\mathcal{I}(n_s) = \mathbf{V}(n_s)\left[1 + \frac{n_s}{F}\right] \tag{8}$$

with F, the number of frequencies and n_s, the model order. The best model order in terms of low model error and weak noise sensitivity corresponds therefore to the minimum of $\mathcal{I}(n_s)$.

4 AUTOMATIC REMOVAL OF SPURIOUS POLES USING A MODAL DOMINANCY INDEX

In most cases, the presence of spurious poles is unavoidable due to noisy data or modelling errors. They have been shown to strongly perturb the estimation of the nonlinear coefficients and the underlying linear properties [8][13][14]. Consequently, a procedure to automatically discriminate spurious from genuine poles and removing them has been established and is described in this section.

Spurious poles are removed from the estimated model through the reduction of the dimensionality of the state space matrices. Those matrices first have to be converted into the modal space using the following transformations

$$\begin{aligned} \mathbf{\Lambda} &= \Phi^{\dagger}\mathbf{A}\Phi = \mathrm{diag}\left(\lambda_1, \lambda_2, ..., \lambda_{n_s}\right) & (9) \\ \hat{\mathbf{C}} &= \mathbf{C}\Phi & (10) \end{aligned}$$

where λ and Φ are the eigenvalues and the matrix of eigenvectors of $\mathbf{A}$, respectively; and $\bullet^{\dagger}$ is the Moore-Penrose pseudo-inverse. Poles considered as spurious can then be removed by suppressing the corresponding diagonal terms and columns in $\mathbf{\Lambda}$ and $\hat{\mathbf{C}}$, respectively. Reduced state matrix $\mathbf{\Lambda}^r \in \mathbb{C}^{n_r \times n_r}$ and reduced output matrix $\hat{\mathbf{C}}^r \in \mathbb{C}^{n_p \times n_r}$ are so obtained. Reduced extended input matrix $\hat{\mathbf{B}}^r \in \mathbb{C}^{n_r \times (s+1) n_p}$ and reduced direct feedthrough matrix $\mathbf{D}^r = \mathbf{D} \in \mathbb{C}^{n_p \times (s+1) n_p}$ are calculated by minimising the weighted difference between the measured and modelled output spectra in a linear least-square sense, *i.e.*

$$\hat{\mathbf{B}}_d^r, \mathbf{D} = \arg\min \sum_{k=1}^{F} \mathbf{W}^2(k) |\mathbf{Y}(k) - \mathbf{G}_d^r(k)\mathbf{E}(k)|^2 \tag{11}$$

where $\mathbf{G}_d^r$ is the transfer function associated with the reduced system. Using the same continuous-to-discrete transformations shown in the previous section, this function is defined as follows, with $z_k = e^{j2\pi k/N}$

$$\mathbf{G}_d^r(k) = \hat{\mathbf{C}}^r \left(z_k \mathbf{I}^{n_r \times n_r} - \mathbf{\Lambda}_d^r\right)^{-1} \hat{\mathbf{B}}_d^r + \mathbf{D} \tag{12}$$

The four matrices $\{\mathbf{\Lambda}_d^r, \hat{\mathbf{B}}_d^r, \hat{\mathbf{C}}^r, \mathbf{D}\}$ constitute the reduced system from which spurious poles have been extracted.

However, that reduction techniques relies on a correct identification of spurious poles. Although visually helpful to discriminate those poles, stabilisation diagrams can be difficult to interpret in presence of high modal density or noisy measurements. In addition, they always requires the analyst's intervention. The use of a modal dominancy index[15] to identify physical poles in a robust and automatic way is presented in this section.

The loss in accuracy due to the reduction can be assessed by inspecting the difference between the responses of the full original system and the reduced one. By means of the transfer functions of the two systems, a modal error transfer function can be calculated as shown in Eq. 13.

$$\mathbf{G}(j\omega) - \mathbf{G}^r(j\omega) = \mathbf{C}\left(j\omega \mathbf{I}^{n_s \times n_s} - \mathbf{A}\right)^{-1} \mathbf{B} - \hat{\mathbf{C}}^r \left(j\omega \mathbf{I}^{n_r \times n_r} - \mathbf{\Lambda}^r\right)^{-1} \hat{\mathbf{B}}^r \tag{13}$$

More particularly, if $\mathbf{G}_i$ is the transfer function of a reduced system where only the i^{th} modal coordinate has been suppressed, it is possible to compute the loss of accuracy due to the exclusion of that specific i^{th} pole. In case $\mathbf{G}^r = \mathbf{G}_i$, the modal error transfer function becomes

$$\mathbf{G}(j\omega) - \mathbf{G}_i(j\omega) = \frac{\hat{\mathbf{c}}_i \hat{\mathbf{b}}_i}{j\omega - \lambda_i} \tag{14}$$

where $\hat{\mathbf{B}} = \Phi^{\dagger}\mathbf{B} = \left[\hat{\mathbf{b}}_1, \hat{\mathbf{b}}_2, ..., \hat{\mathbf{b}}_{n_s}\right]^T$ and $\hat{\mathbf{C}} = \mathbf{C}\Phi = \left[\hat{\mathbf{c}}_1, \hat{\mathbf{c}}_2, ..., \hat{\mathbf{c}}_{n_s}\right]$. To measure the distance between two systems, the $\mathcal{H}_2$ norm may prove useful. Moreover, for estimation of the system dynamics within a specific bandwidth, this norm can be restricted in frequency by setting proper limits of integration. Definitions of the $\mathcal{H}_2$ norm and the frequency-restricted $\mathcal{H}_2$ norm in a range $[\omega_1,\ \omega_2]$ are shown in Eq. 15 and Eq. 16, respectively.

$$\|\mathbf{G}(j\omega)\|_{\mathcal{H}_2} = \left(\frac{1}{2\pi}\int_{-\infty}^{\infty} \|\mathbf{G}(j\omega)\|_{\mathrm{F}}^2 d\omega\right)^{\frac{1}{2}} = \left(\frac{1}{2\pi}\int_{-\infty}^{\infty} \mathrm{trace}\left[\mathbf{G}^{\mathrm{H}}(j\omega)\mathbf{G}(j\omega)\right] d\omega\right)^{\frac{1}{2}} \tag{15}$$

$$\|\mathbf{G}(j\omega)\|_{\mathrm{FR}\mathcal{H}_2} = \left(\frac{1}{2\pi}\int_{\omega_1}^{\omega_2} \mathrm{trace}\left[\mathbf{G}^{\mathrm{H}}(j\omega)\mathbf{G}(j\omega)\right] d\omega + \frac{1}{2\pi}\int_{-\omega_2}^{-\omega_1} \mathrm{trace}\left[\mathbf{G}^{\mathrm{H}}(j\omega)\mathbf{G}(j\omega)\right] d\omega\right)^{\frac{1}{2}} \tag{16}$$

where $\| \bullet \|_{\mathbf{F}}$ and $\bullet^{\mathrm{H}}$ are the Frobenius norm and the Hermitian transpose, respectively. By applying that frequency-restricted $\mathcal{H}_2$ norm to the modal error transfer function of Eq. 14, a so-called Frequency-Restricted $\mathcal{H}_2$-based Modal Dominancy Index is constructed. Explicit form of that index is given in Eq. 18.

$$\begin{aligned}
\mathrm{MDI}_{\;i} &= \|\mathbf{G}(j\omega) - \tilde{\mathbf{G}}_i(j\omega)\|^2_{\mathrm{FR}\mathcal{H}_2} && (17) \\
&= \frac{1}{\pi}\mathrm{trace}\left[\hat{\mathbf{b}}_i^{\mathrm{H}}\hat{\mathbf{c}}_i^{\mathrm{H}}\hat{\mathbf{c}}_i\hat{\mathbf{b}}_i\right]\left[\frac{1}{|\mathrm{Re}\,(\lambda_i)\,|}\arctan\left(\frac{\omega}{|\mathrm{Re}\,(\lambda_i)\,|}\right)\right]_{\omega_1-|\mathrm{Im}(\lambda_i)|}^{\omega_2-|\mathrm{Im}(\lambda_i)|} && (18)
\end{aligned}$$

If a physical mode has an important modal contribution, its exclusion will significantly impact the response of the new system and hence increase the difference with the original one. Therefore, physical poles exhibit high modal dominancy index (MDI) whereas spurious poles have low MDI as they contribute weakly to the system dynamics. Given an appropriate threshold for the MDI, identified poles can then be automatically and effectively classified.

5 VALIDATION ON A SATELLITE STRUCTURE EXHIBITING STRONGLY NONLINEARITIES

The established procedure is applied in this section to a complete satellite structure known to be prone to strong nonlinear mechanisms and possessing a high modal density[5] [16] [17].

5.1 DESCRIPTION AND MODELLING OF THE SMALLSAT SPACECRAFT

The SmallSat structure was conceived by EADS-Astrium as a low-cost platform for small satellites in low earth orbits[18]. It is a monocoque tube structure which is $1.2m$ in height and $1m$ in width and weights around $64kg$. It incorporates eight flat faces for equipment mounting purposes, creating an octagon shape, as shown in Figure 3a. The octagon is made in carbon-fibre-reinforced polymer covered by a skin of Kevlar. The interface between the spacecraft and launch vehicle is achieved via four aluminium brackets located around cut-outs at the base of the structure.

The spacecraft structure supports a dummy telescope mounted on a baseplate through a tripod; its mass is around $140kg$. The dummy telescope plate is connected to the SmallSat top floor by three shock attenuators, termed Shock Attenuation System for Spacecraft and Adaptor (SASSA), whose behaviour is considered as linear in this study. Besides, as depicted in Figure 3c, a support bracket connects to one of the eight walls the so-called Wheel Elastomer Mounting System (WEMS) device which is loaded with an $8-kg$ dummy inertia wheel. The WEMS device is a mechanical filter which mitigates disturbances coming from the inertia wheel through the presence of a soft elastomeric interface between its mobile part, i.e. the inertia wheel and a supporting metallic cross, and its fixed part, i.e. the bracket and by extension the spacecraft. Moreover, eight mechanical stops limit the axial and lateral motions of the WEMS mobile part during launch, which gives rise to strongly nonlinear dynamical phenomena. Figure 3d presents a simplified though relevant modelling of the WEMS device where the inertia wheel is seen as a point mass. The four nonlinear connections (NCs) between the WEMS mobile and fixed parts are labelled NC 1 4. Each NC possesses a trilinear spring in the axial direction (elastomer in traction/compression plus two stops), a bilinear spring in the radial direction (elastomer in shear plus one stop) and a linear spring in the third direction (elastomer in shear). In Figure 3d, linear and nonlinear springs are denoted by squares and circles, respectively.

A finite element model (FEM) of the SmallSat was developed to conduct numerical experiments. It comprises about $65,000$ DOFs and the comparison with experimental data revealed its good predictive capabilities. The model consists of shell elements (octagon structure and top floor, instrument baseplate, bracket and WEMS metallic cross) and point masses (dummy inertia wheel and telescope) and meets boundary conditions with four clamped nodes, as shown in Figure 3b. Structural damping is considered by means of the proportional damping rule and the high dissipation in the elastomer components of the WEMS is described using lumped dashpots, hence resulting in a highly non-proportional damping matrix. Table 1 gives the natural frequencies ω and damping ratios ζ of the first 11 modes of the SmallSat up to $50Hz$.

To achieve tractable nonlinear calculations, the linear elements of the FEM were condensed using the Craig-Bampton reduction technique. Specifically, the full-scale model of the spacecraft was reduced to 13 nodes (excluding DOFs in rotation), namely both sides of each NC (8), the inertia wheel point mass (1) and the four corners of the instrument baseplate (4), and 100 modes. In total, the reduced-order model thus contains 139 DOFs. Nonlinearity was finally introduced within the WEMS module

Mode	Natural frequency ω $[Hz]$	Damping ratio ζ $[\%]$	Description
1	10.67	5.34	Concave motion of the WEMS mobile part (WMP) along X
2	11.01	5.58	Symmetric to mode 1 along Y
3	28.26	9.79	Convex motion of the WMP along X
4	28.41	10.62	Symmetric to mode 3 along Y
5	30.11	7.03	Bracket bending and in-phase motion of the WMP along X
6	30.52	15.54	Rotation of the WMP around Z
7	31.59	2.07	Rotation of the instrument panel (IP)
8	32.62	2.25	Rotation of the IP perpendicularly to mode 7 and motion of the WMP along Z
9	37.47	2.27	Rotation of the IP similarly to mode 8 and rotation around Z
10	38.26	2.33	Main structure bending and in-plane motion of the IP in phase
11	48.31	2.51	Rotation of the IP similarly to mode 8

TABLE 1: Natural frequencies and damping ratios of the first 11 modes of the SmallSat up to $50Hz$ and description of the corresponding deformations of the structure

between the NC nodes given eight piecewise-linear springs whose parameters were accurately identified from measurements data recorded under sine-sweep excitation using the restoring force surface method[5]. For instance, the stiffness curve at NC1, is depicted in Figure 2.

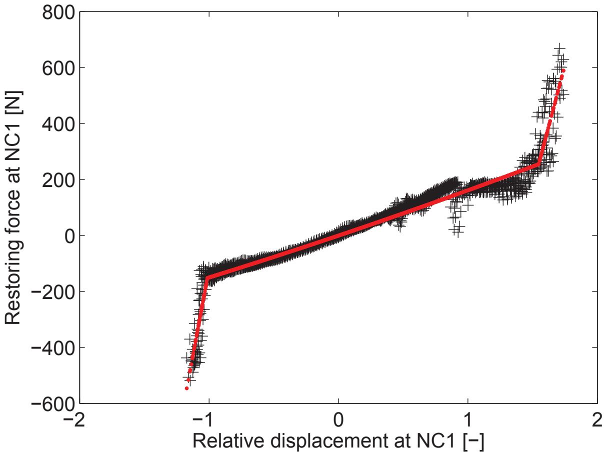

Figure 2: Experimental stiffness curve of NC1 constructed using the restoring force surface method (in black) and fitted with a trilinear model (in red).

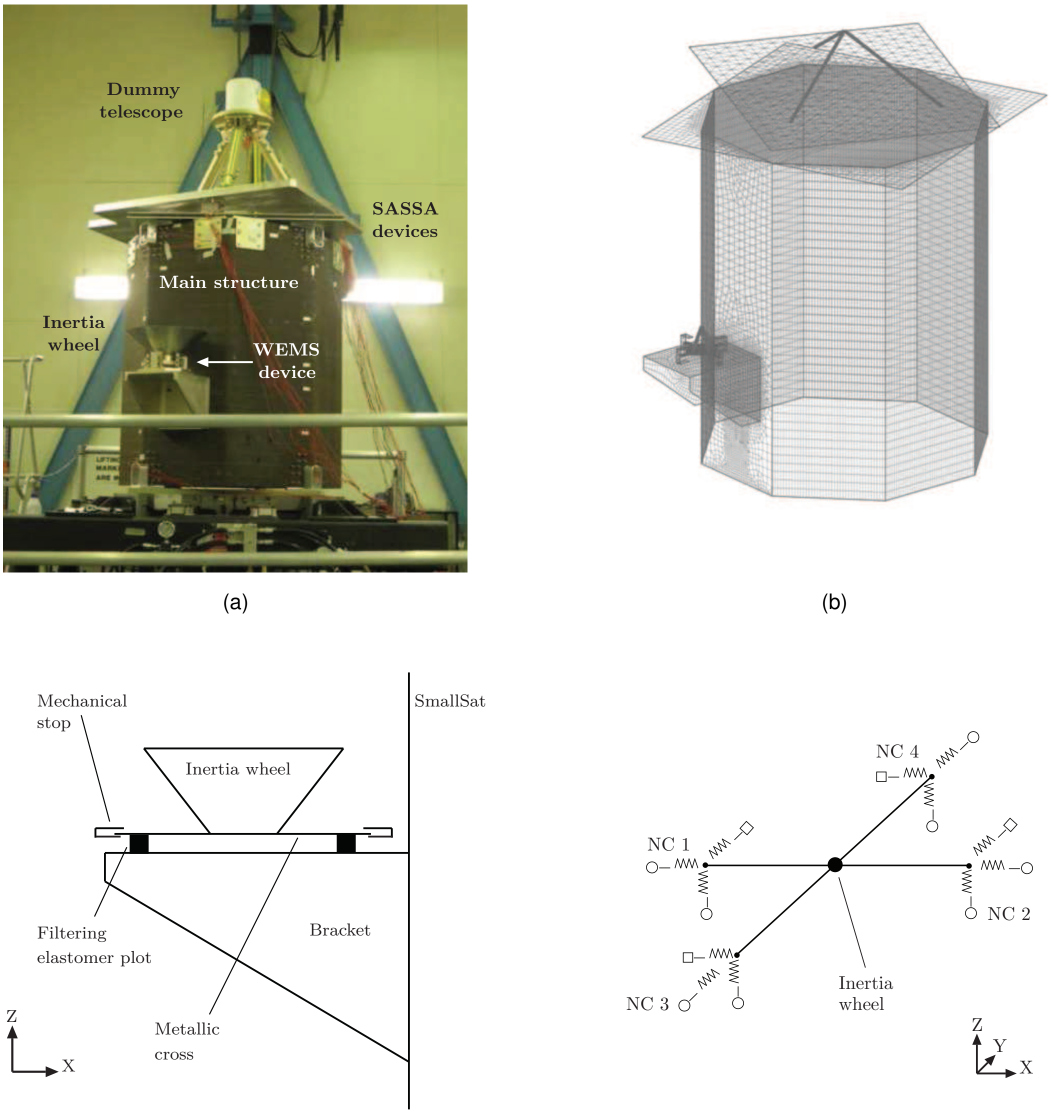

(a) (b)

(c) (d)

Figure 3: SmallSat spacecraft equipped with an inertia wheel supported by the WEMS and a dummy telescope connected to the main structure by the SASSA isolators. (a) Photograph. (b) Finite-element model. (c) Detailed description of the WEMS components. (d) Simplified modelling of the WEMS mobile part considering the inertia wheel as a point mass. The linear and nonlinear connections between the WEMS mobile and fixed parts are signalled by squares and circles, respectively. (e)Experimental stiffness curve of NC1 constructed using the restoring force surface method (in black) and fitted with a trilinear model (in red).

5.2 NUMERICAL SIMULATION TO ACTIVATE NONLINEAR MECHANISMS IN THE WEMS DEVICE

A multisine excitation with a flat amplitude spectrum and a root-mean-squared (RMS) amplitude of $100N$ was applied in the axial direction to NC 2 on the inertia wheel side. The excited band was limited to $550Hz$ to encompass the linear modes of interest. Time integration was carried out using a nonlinear Newmark algorithm with a sampling rate of $20000Hz$, and the time histories were low-passed filtered prior to being decimated down to $1000Hz$. The SmallSat response was simulated over 6 periods of 8192 samples, 5 periods of which were discarded to achieve steady-state conditions. The choice of a relatively low number of periods is explained by the unnecessary need to average the measurements in the absence of noise. The amplitude and the location of the excitation caused impacts exclusively on the negative and positive mechanical stops of NC 2. In the application of the FNSI method, measured frequency lines are processed in $5250Hz$ to capture the contributions appearing outside the input band due to nonlinearities.

5.3 SUBSPACE IDENTIFICATION PROCESSING OF THREE MEASURED CHANNELS WITH ROBUST MODEL ORDER SELECTION

A first identification of the satellite structure using the FNSI method is performed by processing only a limited number of measured channels. It is indeed interesting to validate the proposed procedure even in extreme cases when the number of available channels is very low. More particularly, 3 out of the 39 measured channels are considered to carry out the identification.

First of all, an appropriate set of basis functions to estimate the nonlinearities has to be selected. A preliminary nonlinear analysis using, for instance, the restoring force surface method[19] on sine-sweep measurements can provide useful insights to achieve this selection. Moreover, such analysis can also lead to accurate estimation of actual clearances of the system (see Figure 2). Therefore, in this paper, the choice is made on trilinear functions where the clearances are assumed to be known and only the stiffness coefficients of the WEMS device remain to identify.

The second step consist in the delicate task of selecting a model order. As previously discussed, though the use of stabilisation diagrams tends to ease the user's task, the order selection may reveal arduous in case of high modal density, noisy data or strong nonlinearities. Consequently, the information criterion proposed in the Section 3 is here computed for model orders starting from 2 to 60 and illustrated in Figure 4. The selection of the model order becomes then straightforward as the optimal order is found at the minimum of the information criterion curve. In this case, an order of 10 can guarantee both a small model error and a low noise sensitivity.

The inspection of the stabilisation diagram in Figure 5 can confirm that the four physical modes visible in the diagram (modes 1,4,6 and 8, see Table 1) are well captured for a model order equal to 10. However, one can observe that those four modes were already included at order 8. For this reason, based on the stabilisation diagram only, selecting an order equal to 8 might appear a better choice at first.

The analysis of the estimated nonlinear coefficients and their frequency-dependence often offers a convenient tool to assess the quality of the identification process. Figure 6 depicts the calculated nonlinear stiffness for order 8, 10 and 12. Although those three orders seem to be very similar in terms of identified poles regarding the stabilisation diagram, strong drift and peaks appearing in the curves of the nonlinear coefficients tends to prove that the identification is of poorer quality in the cases of order 8 or 12. Same conclusion can be drawn from the Table 2. Whereas the error does not allow to discern a better order as the value of the coefficient is averaged over the frequencies, standard deviation and real-to-imaginary part ratio indicate a better identification for order 10. The optimal order given by the information criterion is thus effectively detected.

Order	NC	Exact value	Real part	Error (%)	Std	Log_{10}(Re/Im)
8	2-Z (neg.)	116.73	116.38	-0.30	1.71	2.37
8	2-Z (pos.)	88.41	89.09	0.76	2.38	2.03
10	2-Z (neg.)	116.73	117.12	0.34	0.54	2.54
10	2-Z (pos.)	88.41	88.32	-0.10	0.78	2.36
12	2-Z (neg.)	116.73	116.96	0.20	2.25	2.15
12	2-Z (pos.)	88.41	88.15	-0.30	2.42	2.11

TABLE 2: Estimations of the NC 2 -Z nonlinear coefficients considering three different model order.

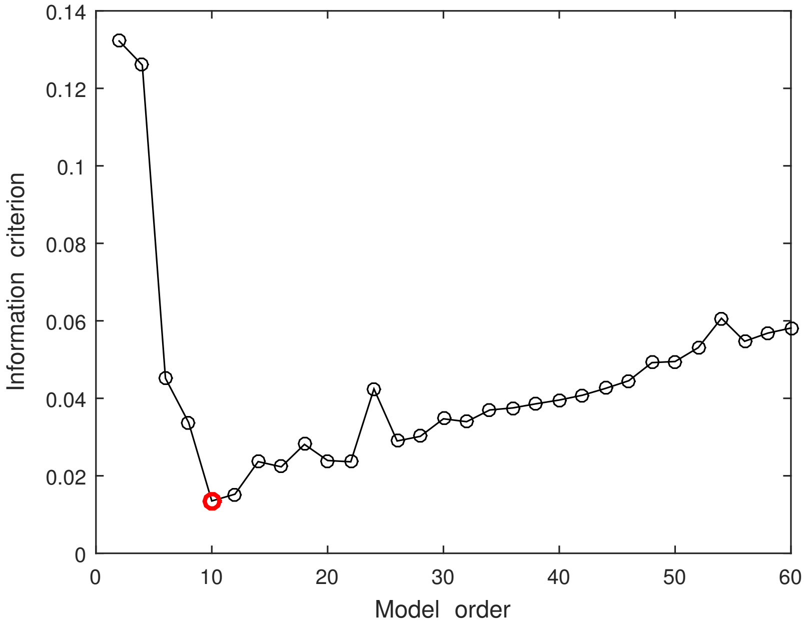

Figure 4: Information criterion computed for orders from 2 to 60 using three measured channels; Red circle: optimal order.

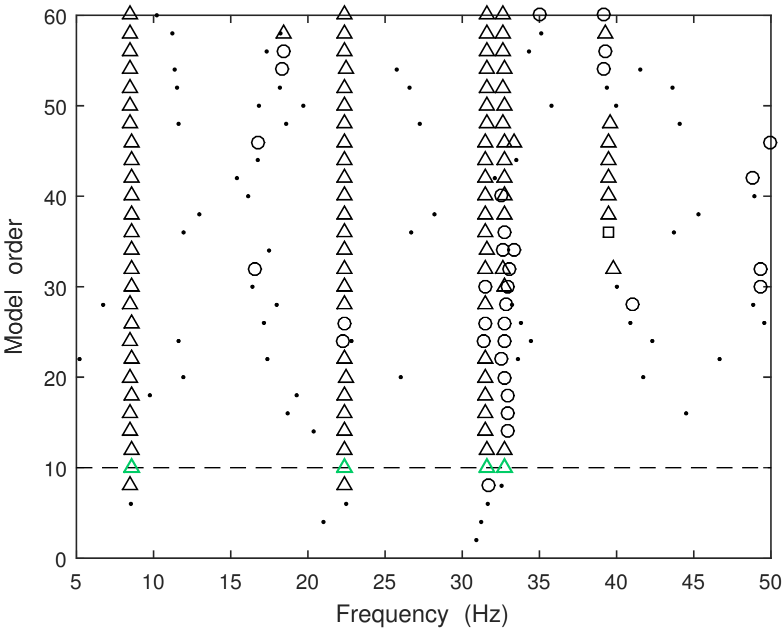

Figure 5: Stabilisation diagram computed using three measured channels. Dot: new pole; cross: stabilisation in natural frequency; square: extra stabilisation in damping ratio; circle: extra stabilisation in MACX; triangle: full stabilisation.

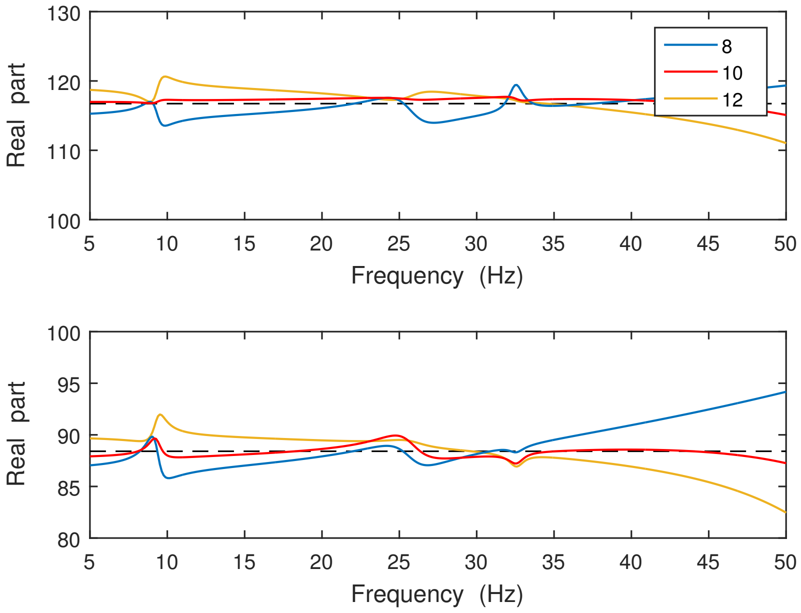

Figure 6: Estimations of the NC 2 -Z nonlinear coefficients considering three different model order. Blue: $n_s = 8$; red: $n_s = 10$; orange: $n_s = 12$; dashed line: exact value

5.4 SUBSPACE IDENTIFICATION PROCESSING OF ALL MEASURED CHANNELS: AUTOMATIC SPURIOUS POLES DETECTION AND MODEL ORDER REDUCTION

The same procedure is then applied for the entirety of measured channels, *i.e.* 39. Though the discontinuity is less pronounced than in Figure 4, reflecting a smoother convergence of the model error, the information criterion exhibits a minimum for an order equal to 22, as shown in Figure 7.

By inspection the stabilisation diagram in Figure 8 and referring to the Table 1, it can be seen that, for a model order of 22, not all the physical modes are identified. For instance, mode 2 and mode 9 only begin to be identified for an order greater or equal to 38 and 36, respectively. But, as those modes must have a low modal contribution to the total response, their inclusion into the model does not improve significantly the quality of the identification. In consequence, the information criterion determines an optimal order at 22 rather than at 38.

Nevertheless, it is sometimes needed to identify all the physical modes in the frequency range of interest, whether having low modal contribution or not. Higher model orders should then be considered, keeping in mind that they imply high noise sensitivity and a larger amount of spurious poles. As those poles tend to deteriorate the overall estimation, they have to be localized and discarded using the automatic procedure introduced in Section 4.

Setting the model order to 38, the modal dominancy index is computed for each identified poles and represented in Figure 9. With the knowledge of physical modes listed in Table 1, one can verify that, modal dominancy indices of physical poles are all greater than the one associated to spurious poles. Consequently, by fixing an appropriate threshold, all the physical poles can be efficiently distinguished from the others and kept in the reduced model.

The negative impact of spurious poles on the estimation of the nonlinear coefficient is seen to be powerfully suppressed in Figure 10, by discarding them from the reduced system. Parasitic peaks appearing at the same frequency as those spurious poles are then efficiently removed, leading to a better estimation of the nonlinear stiffness. Remaining peaks in the nonlinear coefficient are not associated to spurious poles but actually correspond to antiresonance frequencies (around 9, 26 and $32 Hz$), as can be verified in Figure 11.

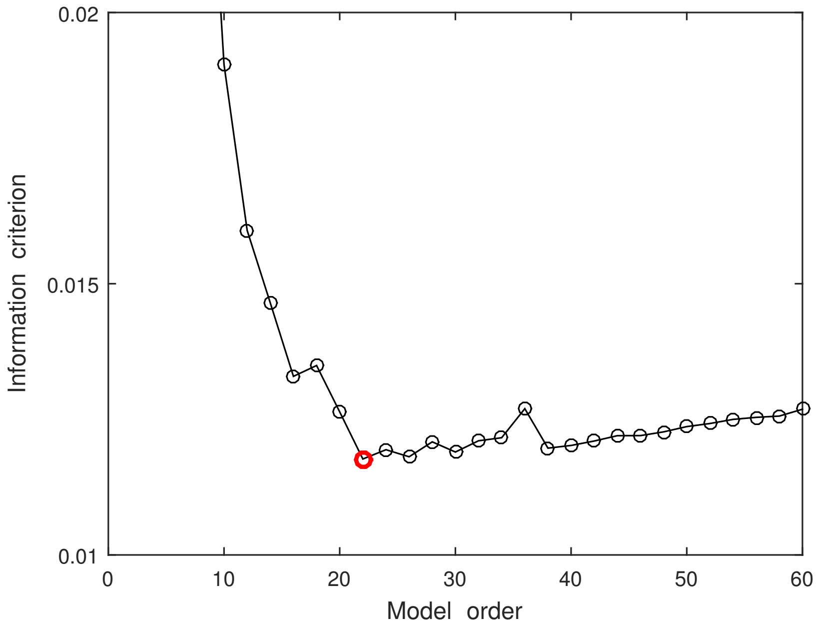

Figure 7: Information criterion computed for orders from 2 to 60 using all measured channels; Red circle: optimal order.

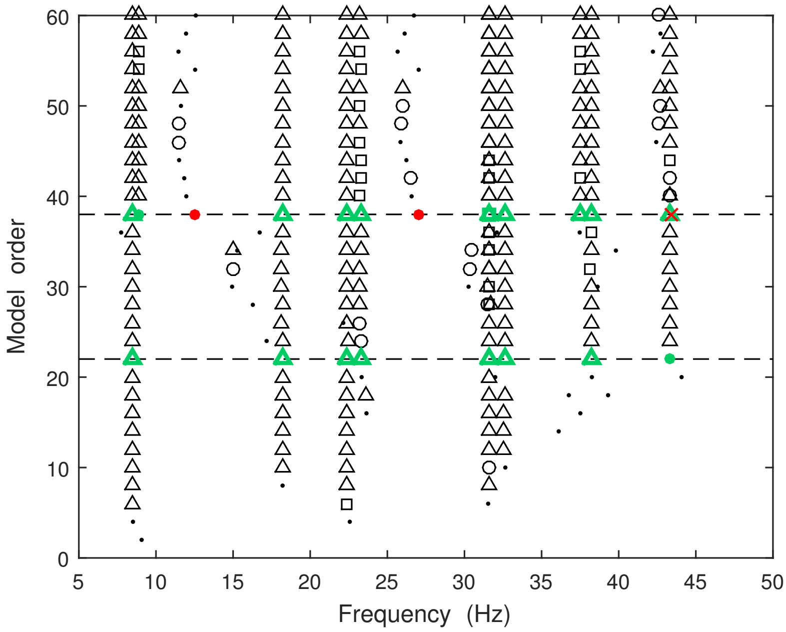

Figure 8: Stabilisation diagram computed using all measured channels. Dot: new pole; cross: stabilisation in natural frequency; square: extra stabilisation in damping ratio; circle: extra stabilisation in MACX; triangle: full stabilisation. Green: physical poles according to the MDI; red: spurious poles according to the MDI. Dashed lines indicate the selected orders.

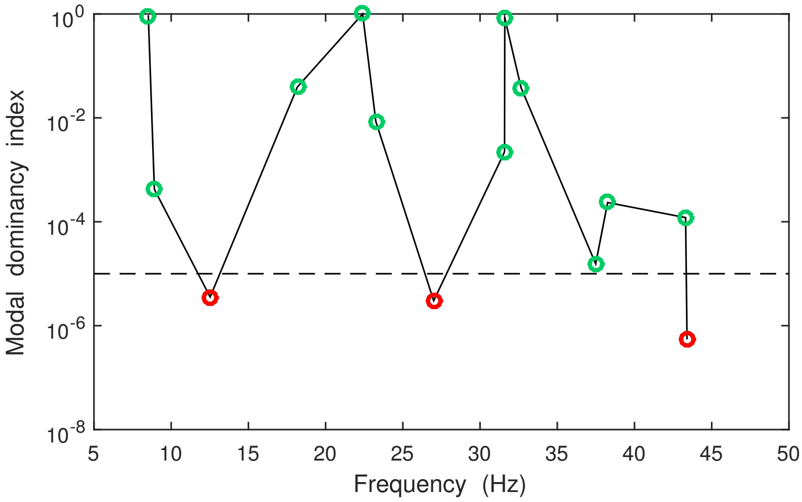

Figure 9: Modal dominancy index of each identified poles at an order equal to 38. Dashed line: set threshold to discard spurious poles; green dots: physical poles; red dots: spurious poles.

On the other hand, the quality of the linear parameters estimation can also be assessed in Figure 11, where frequency response functions at the driving point are represented. The black curve is the FRF obtained at low level ($1N$ RMS) where no nonlinearity is activated, the blue curve is the underlying linear FRF synthesised by FNSI at high level ($100N$ RMS) using an efficient decoupling of the linear and the nonlinear contributions. By means of Eq. 6, the red curve is computed at high level to emphasize the strong impact of the nonlinear distortions on the satellite dynamics.

Finally, a comparison is performed with a similar modal dominancy index but based on a different norm, the $\mathcal{H}_\infty$-based Modal Dominancy Index. Starting from Eq. 14, a different measure of the distance between the two systems (the original and the system reduced by extracting one specific pole) is performed through the use of $\mathcal{H}_\infty$ norm[20].

$$\mathrm{MDI}_i^{\infty} = \|\mathbf{G}(j\omega) - \tilde{\mathbf{G}}_i(j\omega)\|_{\mathcal{H}_\infty} \tag{19}$$

$$= \left\| \frac{\hat{\mathbf{c}}_i \hat{\mathbf{b}}_i}{j\omega - \lambda_i} \right\|_{\mathcal{H}_\infty} = \frac{\max\left(\mathrm{svd}\left(\hat{\mathbf{c}}_i \hat{\mathbf{b}}_i\right)\right)}{|\mathrm{Re}\,(\lambda_i)\,|} \tag{20}$$

where $\mathrm{svd}(\bullet)$ stands for the singular values of $\bullet$. The ratio between the lowest physical pole and the highest spurious one in terms of modal dominancy index represents a measure of the range where a threshold can be safely set. For a model order of 38, this ratio is equal to 4.35 with the $\mathcal{H}_2$-based index and to 1.15 with the $\mathcal{H}_\infty$-based index. The margin is thus very narrow in the case of $\mathcal{H}_\infty$, as illustrated in Figure 12 where the horizontal dashed-line setting the threshold must lie between the third (spurious) and the eleventh (physical) identified poles. The use of $\mathcal{H}_2$ appears therefore more robust as the separation between the two classes is clearer.

Moreover, this index is particularly suitable when highly non proportional damping mechanisms are involved as classical modal validation criteria such as the modal assurance criterion, the modal phase collinearity or the mean phase deviation have been shown to fail in case of non proportional damping.

6 CONCLUSION

The goal of this paper was to develop a robust procedure to identify complex structures possessing strong nonlinearities and high modal density. Indeed, in such cases, the identification process is made difficult through the selection of an optimal model order and the unavoidable presence of spurious poles captured by the model for high orders. For this purpose, the frequency-domain subspace identification method (FNSI) was improved by means of techniques allowing first, a robust and automatic model order selection, and secondly, the discrimination and the removal of spurious poles from the estimated model.

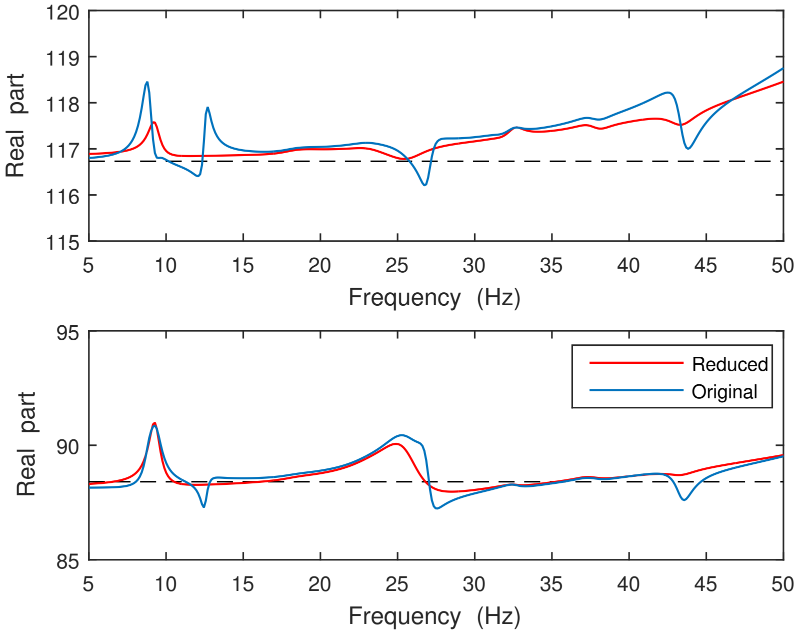

Figure 10: Estimations of the NC 2 -Z nonlinear coefficients using all measured channels. Blue: considering all poles; red: after removal of spurious poles.

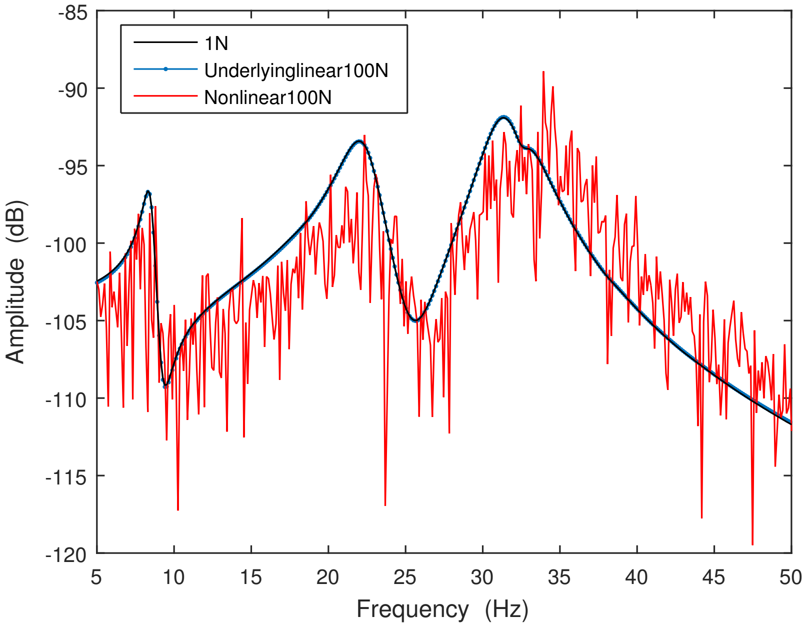

Figure 11: Driving-point FRF. Black: obtained at low level (no nonlinearity); blue: synthesised using FNSI at high level (extraction of underlying linear properties); red: at high level using Eq. 6.

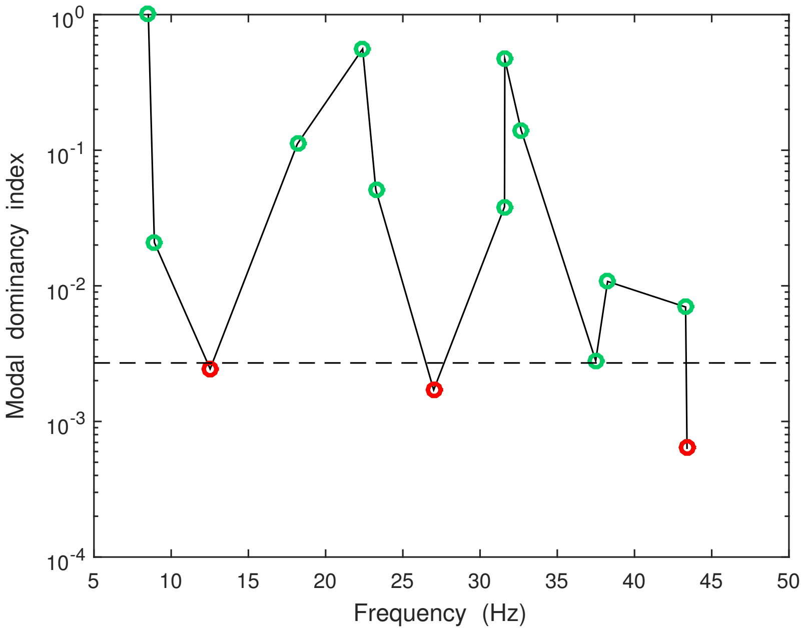

Figure 12: Infinity-norm-based modal dominancy index of each identified poles at an order equal to 38. Green: physical poles; red: spurious poles. Dashed line: set threshold to discard spurious poles.

An information criterion based on the actual model error and the noise sensitivity was introduced. Though very helpful, the use of stabilisation diagrams only for model order selection can lead to a suboptimal choice. Indeed, the user can be misled and opting either for too low model order by not taking into account modes laying outside of the frequency range, or either for too high model order by uselessly selecting physical modes with very low modal contribution.

A modal dominancy index was then adapted to the FNSI method to provide a reliable criterion for distinguishing physical from spurious poles. Modal truncation procedure was also introduced to reduce the system by removing those spurious poles.

The whole identification procedure was successfully applied to a satellite structure, the Smallsat, possessing nonsmooth nonlinearities and a high modal density. The use of the information criterion enabled a straightforward selection of an optimal model order, leading to a better estimation of the parameters than a classical use of stabilisation diagrams. In addition, it was shown that Spurious poles were properly identified using the modal dominancy index and removed by model reduction, leading to a better estimation of the nonlinear coefficients.

ACKNOWLEDGEMENTS

The authors T. Dossogne and J.P. Noël are Research Fellow (FRIA fellowship) and Postdoctoral Researcher, respectively, of the *Fonds de la Recherche Scientifique* FNRS which is gratefully acknowledged.

REFERENCES

[1] **Bowden, M.** and **Dugunji, J.**, *Joint damping and nonlinearity in dynamics of space structures*, AIAA Journal, Vol. 24, No. 4, pp. 740–749, 1990.

[2] **Wei, F.** and **Zheng, G.**, *Nonlinear vibration analysis of spacecraft with local nonlinearity*, Mechanical Systems and Signal Processing, Vol. 24, No. 2, pp. 481–490, 2010.

[3] **Okuizumi, N.** and **Natori, M.**, *Nonlinear Vibrations of a Satellite Truss Structure with Gaps*, *45th*

AIAA/ASME/ASCE/AHS/ASC Structures, Structural Dynamics and Materials Conference, Palmsprings, USA, 2004.

[4] **Carney, K., Yunis, I., Smith, K.** and **Peng, C.**, *Nonlinear dynamic behavior in the Cassini spacecraft modal survey*, *Proceedings of the International Modal Analysis Conference (IMAC)*, Orlando, USA, 1997.

[5] **Noël, J.-P., Renson, L.** and **Kerschen, G.**, *Complex dynamics of a nonlinear aerospace structure: Experimental identification and modal interactions*, Journal of Sound and Vibration, Vol. 33, No. 1, pp. 2588–2607, 2014.

[6] **Link, M., Boeswald, M., Laborde, S., Weiland, M.** and **Calvi, A.**, *Non-linear experimental modal analysis and application to satellite vibration test data*, *Proceedings of the 3rd International Conference on Computational Methods in Structural Dynamics and Earthquake Engineering*, Corfou, Greece, 2011.

[7] **Noël, J.-P.** and **Kerschen, G.**, *Frequency-domain subspace identification for nonlinear mechanical systems*, Mechanical Systems and Signal Processing, Vol. 40, pp. 701–717, 2013.

[8] **Noël, J.-P., Marchesiello, S.** and **Kerschen, G.**, *Subspace-based identification of a nonlinear spacecraft in the time and frequency domains*, Mechanical Systems and Signal Processing, Vol. 43, pp. 217–236, 2014.

[9] **Noël, J.-P., Kerschen, G., Foltête, E.** and **Cogan, S.**, *Grey-box identification of a nonlinear solar array structure using cubic splines*, International Journal of Non-linear Mechanics, Vol. accepted for publication, 2014.

[10] **Adams, D.** and **Allemang, R.**, *A frequency domain method for estimating the parameters of a non-linear structural dynamic model through feedback*, Mechanical Systems and Signal Processing, Vol. 14, pp. 637–656, 2000.

[11] **Pintelon, R.** and **Schoukens, J.**, System Identification: A Frequency Domain Approach, IEEE Press, Piscataway, NJ, 2001.

[12] **Javier Caraa, F., Juana, J., Alarconb, E., Reynders, E.** and **De Roeck, G.**, *Modal contribution and state space order selection in operational modal analysis*, Mechanical Systems and Signal Processing, Vol. 38, No. 1, pp. 276–298, 2013.

[13] **De Filippis, G., Noël, J.-P., Kerschen, G., Soria, L.** and **Stephan, C.**, *Experimental nonlinear identification of an aircraft with bolted connections*, *Proceedings of the 33th International Modal Analysis Conference (IMAC)*, Orlando, FL, 2015.

[14] **Marchesiello, S., Fasana, A.** and **Garibaldi, L.**, *Modal contributions and effects of spurious poles in nonlinear subspace identification*, Mechanical Systems and Signal Processing, pp. –, 2015.

[15] **Khorsand Vakilzadeh, M., Rahrovani, S.** and **Abrahamsson, T.**, *An improved modal approach for model reduction based on input-output relation*, *Proceedings of the International Conference on Noise and Vibration Engineering (ISMA)*, Leuven, Belgium, 2012.

[16] **Renson, L., Noël, J.-P.** and **Kerschen, G.**, *Complex dynamics of a nonlinear aerospace structure: Numerical continuation and normal modes*, Nonlinear Dynamics, Vol. accepted for publication, 2014.

[17] **Detroux, T., Renson, L., Masset, L., Noël, J.-P.** and **Kerschen, G.**, *Bifurcation analysis of a spacecraft structure using the harmonic balance method*, *Proceedings of the ASME 2015 International Design Engineering Technical Conferences*, Boston, USA, 2015.

[18] **Russell, A.**, *Thick skin, faceted, CFRP, monocoque tube structure for smallsats*, *Proceedings of the European Conference on Spacecraft Structures, Materials and Mechanical Testing*, European Space Agency, Noordwijk, The Netherlands, 2000.

[19] **Masri, S.** and **Caughey, T.**, *A nonparametric identification technique for nonlinear dynamic problems*, Journal of Applied Mechanics, Vol. 46, No. 1, pp. 433447, 1979.

[20] **Rommes, J.** and **Martins, N.**, *Efficient computation of multivariable transfer function dominant poles using subspace acceleration*, IEEE Transaction on Power Systems, Vol. 21, No. 1, pp. 1471–1483, 2006.